Contents

List of Figures

Appendix A

The single dish spectrum of NGC 1052

NGC 1052 is variable at all frequencies observations have been carried out at so far. Variations occur on timescales of months with a tendency of shorter timescales at higher frequencies. For this, it is difficult to obtain a complete source spectrum, since the observations have to be done quasi-simultaneously.

Between August 2001 and March 2002 several flux density measurements of NGC 1052 have been carried out within the scope of this thesis. 9 data points have been obtained with the Effelsberg 100 m telescope between 1.4 and 30 GHz. At 100 and 230 GHz (3 and 1.3 mm) the source flux density has been determined with the Pico Veleta 30 m telescope. Table A.1 lists the available measurements and the obtained spectrum is plotted in Figure A.1.

Table A.1: Flux density measurements of NGC 1052

Frequency	Wavelength	Date	Flux density	Telescope
1.4 GHz	21 cm	18.3.2002	1.40± 0.01 Jy	Effelsberg[a]
1.66 GHz	18 cm	29.8.2001	1.474± 0.020 Jy	Effelsberg[a]
4.85 GHz	6 cm	4.9.2001	1.471± 0.009 Jy	Effelsberg[a]
4.85 GHz	6 cm	10.12.2001	1.463± 0.010 Jy	Effelsberg[a]
8.55 GHz	3.5 cm	8.1.2002	1.40± 0.01 Jy	Effelsberg[a]
10.45 GHz	2.8 cm	10.12.2001	1.378± 0.010 Jy	Effelsberg[a]
22 GHz	1.3 cm	8.1.2002	940± 20 mJy	Effelsberg[a]
22 GHz	1.3 cm	1.2.2002	815.5± 61.7 mJy	Effelsberg[a]
30 GHz	1 cm	26.3.2002	790± 40 mJy	Effelsberg[a]
100 GHz	3 mm	18.9.2001	600±30 mJy	Pico Veleta[b]
230 GHz	1.3 mm	9.12.2001	200±40 mJy	Pico Veleta[c]

[a] performance of the measurements by Dr. A. Kraus; [b] performance of the observation by Dr. H. Ungerechts; [c] performance of the observation by J. Kaufmann

Although it has to be kept in mind that these single dish measurements have been done in winter 2001/2002, about 3 years after the VLBA observations in December 1998, the obtained single dish spectrum can give valuable additional information for the correct interpretation of the VLBI data.

The spectrum appears nearly flat up to $\sim$10 GHz. Between 10 and 22 GHz it turns over and becomes steep. Since no data are available between these frequencies, the exact turnover frequency cannot be located more precisely. Between 10 and 22 GHz the spectral index is -0.6, the spectrum becoming flatter between 22 and 100 GHz ($\alpha_{22-100} \sim -0.25$).

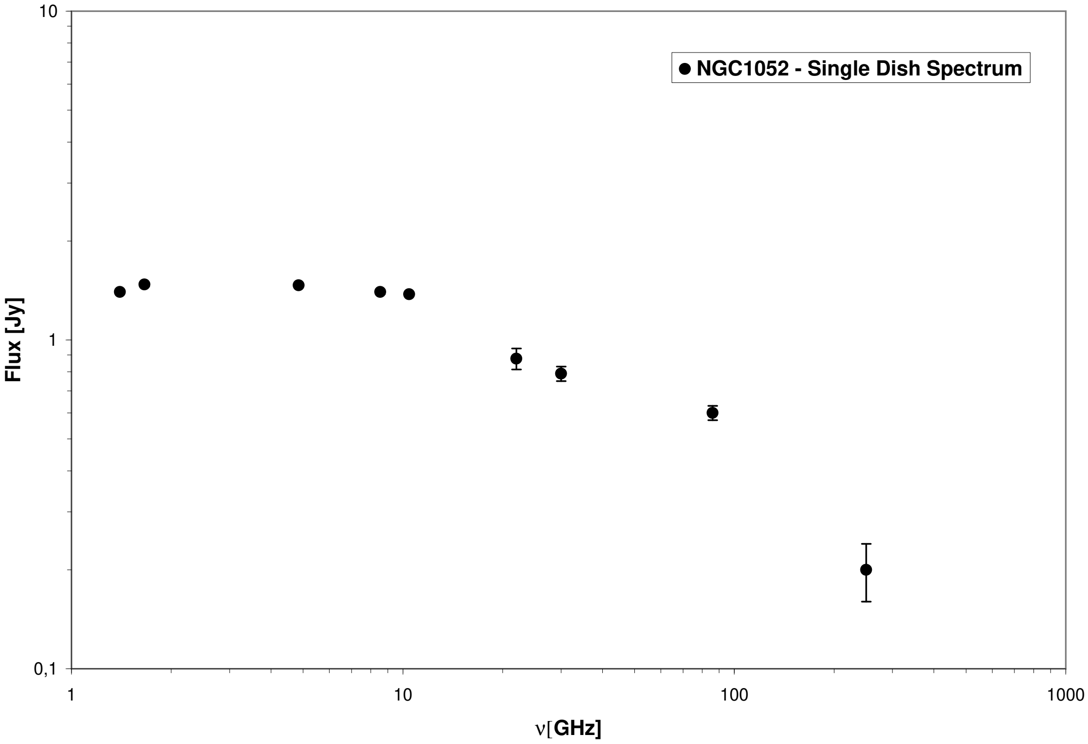

Figure A.1: Single dish spectrum of NGC 1052, measured between August 2001 and March 2002.

It is interesting to note that the VLBI spectrum (from December 1998) turns over in the same regime between 8.4 and 22 GHz and that this could be attributed mainly to the strong decrease of the flux density from the eastern jet compare Figure 4.8. The brightness temperature distribution (Section 4.4) revealed that free-free absorption starts inwards of 3 mas from the central engine, a region of the jet with local turnover frequencies above 8.4 GHz. The sharp cutoff of the single dish spectrum above 10 GHz thus can be interpreted as free-free absorption of the inner jet-regions of the bright, approaching eastern jet, by a stationary obscuring torus. In this picture, the counterjet contributes only an negligible fraction to the registered flux density below 10 GHz, since it is much stronger affected by the obscuration. This explains the flatness of the single-dish spectrum below 10 GHz, which is typical for a one–sided pc–scale jet. Above 10 GHz the inner part of the eastern jet should maintain the flat spectrum, but the edge of the absorber cuts off the spectrum at this point. This interpretation can be tested in a long-term monitoring of the spectrum of NGC 1052. Even if the overall shape of the spectrum varies with time, the cutoff between 10 and 22 GHz should remain a stationary feature of the source-spectrum.

At even higher frequencies (>100 GHz) the spectrum becomes very steep ($\alpha_{100-230} \sim -1.3$). This can be understood in terms of a lack of high energy (synchrotron producing) electrons. If a magnetic field of 60 mG is assumed, a cutoff in the electron energy distribution above $\gamma =\sim 1300$ can be estimated from Equation (2.6). This high value is indeed needed, if the strong and compact X-ray emission from the core of NGC 1052 shall be interpreted in terms of the SSC model (compare Equation 2.12).

Appendix B

MERLIN and CHANDRA observations and data reduction

In this section the radio interferometer MERLIN and the X-ray satellite CHANDRA will be introduced. Both facilities have been used to study the structure of NGC 1052 on kpc–scales in order to visualize more completely the source as a whole than offered by VLBI studies of the radio core alone. Especially spectroscopy of the compact X-ray core in connection with high resolution VLBI imaging is capable of giving a much deeper insight into the physical processes at work in the very vicinity of the central engine. Since VLBI is not sensitive to the emission from the jets on kpc–scales, radio interferometric observations with smaller baselines (as offered by MERLIN) are needed to connect the extended X-ray emission detected by CHANDRA to the radio regime. The data from both facilities have been obtained from public archives and the observations and the data reduction are presented in this chapter The results are presented and discussed in Appendix C and D.

MERLIN data: MERLIN stands for **M**ulti-**E**lement **R**adio-**L**inked **I**nterferometer **N**etwork, a telescope array consisting of 8 individual antennas connected by microwave links and thus forming an aperture synthesis radio telescope with a biggest baseline of about 217 km. MERLIN is capable of observing in full polarimetric mode and its resolution (40 mas at 6 cm wavelength) lies in the middle between the resolutions obtained with VLBI and connected arrays as the VLA. Observations can be done between 151 MHz and 22 GHz with corresponding angular resolutions between 1.4 arcsec and 8 mas. The array consists of the 76 m Lovell telescope and the 37×25 m Mk2 telescope at Jodrell Bank, three 25 m dishes, of the same design as the VLA antennas, located at Tabley and Darnhall in Cheshire and Knockin in Shropshire, another 25 m antenna at Defford in Worcestershire, a second elliptical 37×25 m dish at Wardle (Mk3 telescope) and the 32 m telescope in Cambridge. The location of the MERLIN antennas is shown in Figure B.1.

Data, older than one year, can be obtained from a public archive, provided by the university of Manchester, the operator of MERLIN. On the MERLIN website[1] a complete catalog of MERLIN observations since 1991 can be searched and the *a–priori* calibrated data, processed in a uniform manner by the MERLIN archivist, can be obtained.

MERLIN observed NGC 1052 on November 22nd 1995 with all 8 antennas of the array at 1.4 GHz. The observation was planned and scheduled by Dr. A. Pedlar. The data, ob-

[1] `http://www.merlin.ac.uk`

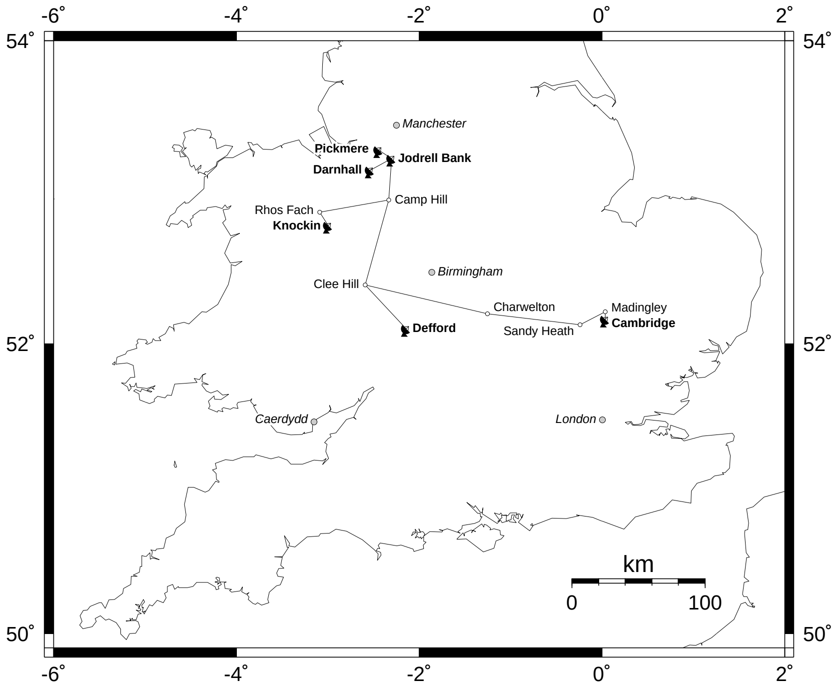

Figure B.1: The antennas of MERLIN

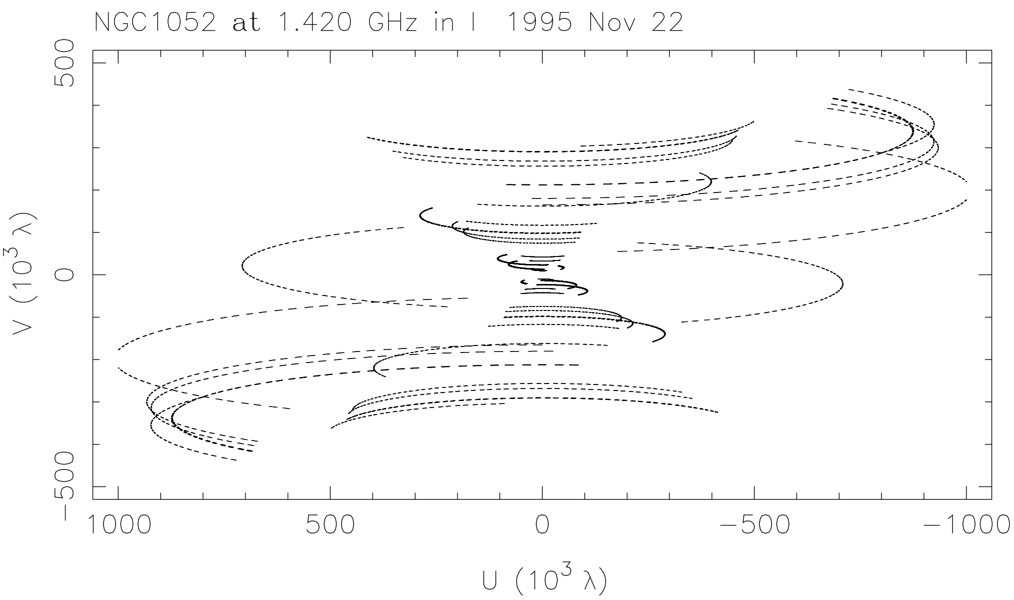

Figure B.2: The (u, v) coverage of the MERLIN observation of NGC 1052.

tained during this experiment, were retrieved from the MERLIN archive with the consent of the principle investigator.

The post-processing of these data was done in DIFMAP. Basically the same strategy as for the mapping and self calibration of the VLBI data, described in Section 3.3, was used with special care on the weighting of the data. Figure B.2 shows the (u, v)-coverage during the observation.

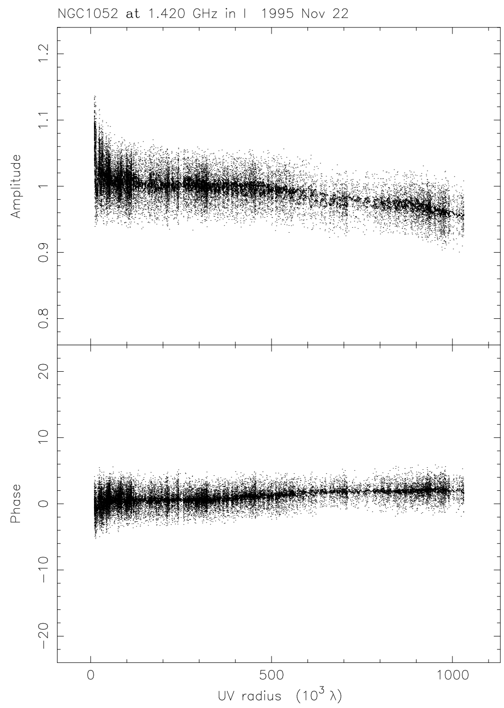

Figure B.3: The visibilities as a function of (u, v) distance and the best model visibilities for the MERLIN observation of NGC 1052.

After a little editing of the data, using the editing option of the commands RADPLOT and VPLOT and the choice of an appropriate map– and cell-size, the mapping was started with natural weighting. After cleaning the central structures, a moderate tapering of the longer baselines revealed more extended emission regions. A strong (u, v)–taper was needed to map the extended lobes of the source, since the synthesized beam of MERLIN at 1.4 GHz is much smaller than these and much of the flux associated with these extended structures would have been resolved out without tapering. After obtaining a good model the data were amplitude self–calibrated, using the command GSCALE, by applying time-independent antenna based correction factors. These factors were 1 without any exception, suggesting a very high quality of the pre-calibrated data. Seven further cycles of cleaning and amplitude calibration were done, each with pure natural weighting for the most compact regions, successively stronger tapering for the more extended regions and decreasing time scales for amplitude self calibration[2]. A final map was produced from the best calibrated data set in two versions, one with the strongest taper applied that had been used during the mapping to show the extended structures of the source, and one with pure natural weighting, showing only the core region of NGC 1052. Figure B.3 shows the visibilities as a function of (u, v)–distance together with the best model, produced with the command RADPLOT. The flatness of the visibility distribution across the (u, v) plane indicates the strong dominance of the central, unresolved core component.

An impression of the quality of the derived model can be obtained by looking at Figure B.4, in which the visibilities on a short (Wardle – Lovell) and a long (Cambridge – Lovell)

[2]A map, produced with uniform weighting for the most compact regions, did not resolve any of the compact features in the natural-weighting-map, but had a higher noise level.

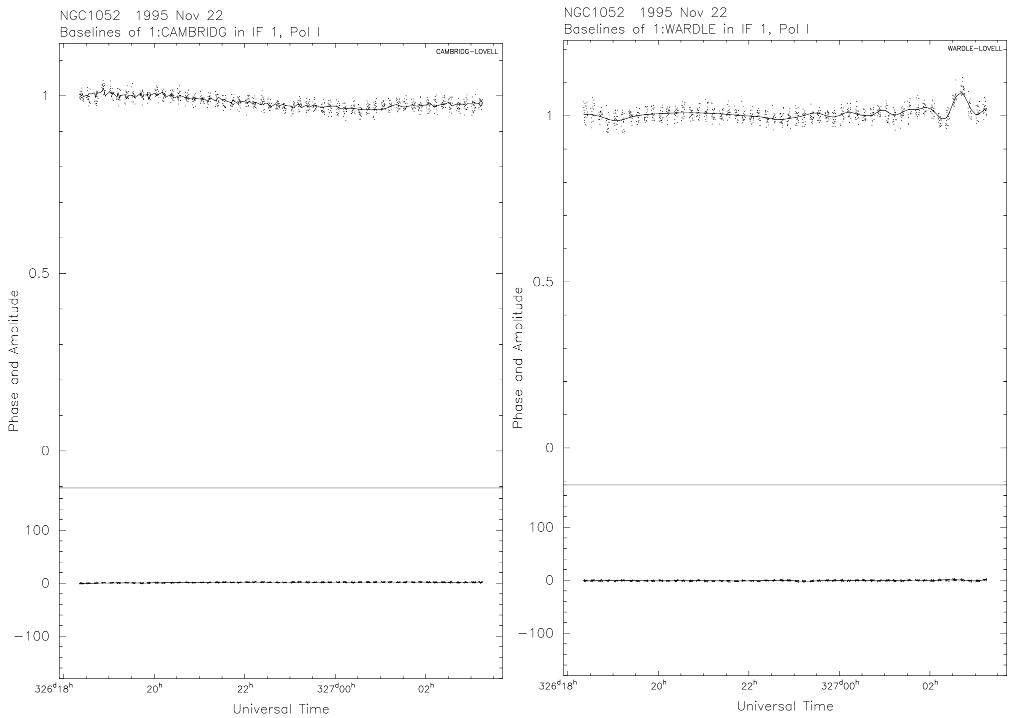

Figure B.4: The visibilities as a function of time for a short (Wardle – Lovell; left panel) and a long (Cambridge – Lovell; right panel) baseline.

baseline as a function of time are shown. The model visibility is seen to lie completely within the scatter of the measured visibilities. The sharp kinks in the model indicate a slight “over modeling” of the data, since a flat curve would probably fit the data nearly as well as the statistically best fit model. However, the deviations are very small and should not affect the final map to a higher degree than introducing spurious features of the same order as the noise level. In Appendix C the final maps are presented and discussed.

CHANDRA data: CHANDRA is one of the most important and efficient X-ray missions of the last and present decade. It has the highest available angular resolution in the X-ray band ($0.5''$), providing the possibility of comparing source structures in the radio (VLA, MERLIN), optical (e.g., the Hubble Space Telescope) and X-ray regime on the same scales. The satellite (Figure B.5) was launched on July 23rd, 1999 and carries a telescope system, consisting of four pairs of mirrors of the Wolter type, which are barrel-shaped and nested (see Figure B.6), focusing incoming X-rays onto a focal plane about 10 m away.

In the focal plane one of two available detectors can be chosen, the **H**igh **R**esolution **C**amera (HRC) and the **A**dvanced **C**CD **I**maging **S**pectrometer (ACIS). Two grating arrays, the low energy transmission grating (LETG) and the high energy transmission grating (HETG) can be flipped into the path of X-rays behind the mirrors for spectroscopy. The CHANDRA data used in this thesis comes from the ACIS detector with no usage of a grating system. For this reason, only the ACIS detector shall be briefly described here.

The ACIS CCD chip array consists of 10 CCD chips divided into two sub-arrays. Four chips make up the ACIS-I array, used for wide-field imaging. It allows a maximal field of view of $16'.9 \times 16'.9$ for each chip with a resolution of $0''.5$, corresponding to a pixel size of $24\,\mu$m. Since the size of the point spread function in the focal plane is of the same order,

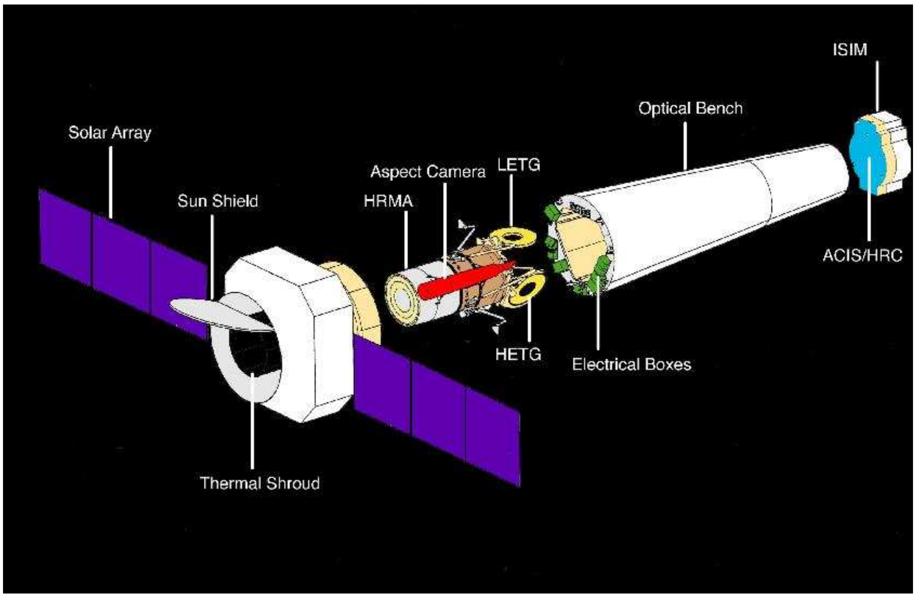

Figure B.5: Components of the CHANDRA satellite. Credits: NASA/CXO/SAO

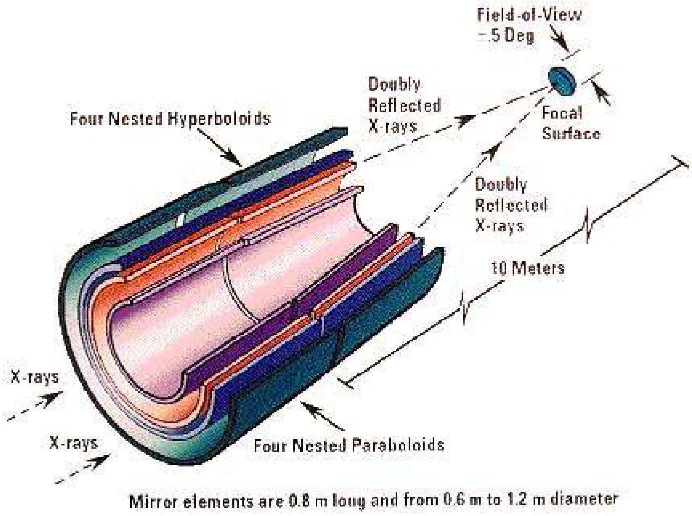

Figure B.6: Illustration of the barrel-shaped mirrors of CHANDRA. Credits: NASA/CXO/SAO

the image from a point-like source is spread over only four pixels. The other six CCD chips make up the ACIS-S array and provide a smaller maximal field of view of $6\times(8'.3\times 8'.3)$ for each chip and provide the same resolution as the ACIS-I chips do. Two of the six ACIS-S chips are illuminated from the back side, providing the best possible sensitivity for soft X-rays. Both arrays are capable of measuring the energy of the incoming X-rays. It is thus possible to retrieve both an image of the source and a spectrum within one observation.

The measured spectra are affected by several instrumental effects that have to be removed in order to retrieve the intrinsic source spectrum. One effect is that the angle for total reflection depends on the energy of the incoming photon ($\Theta_c \propto E^{-1}$). Since the focusing angle spans only a small range for a single mirror, this means that photons with the "wrong" energy are not as efficiently focused as photons with the "right" energy are.

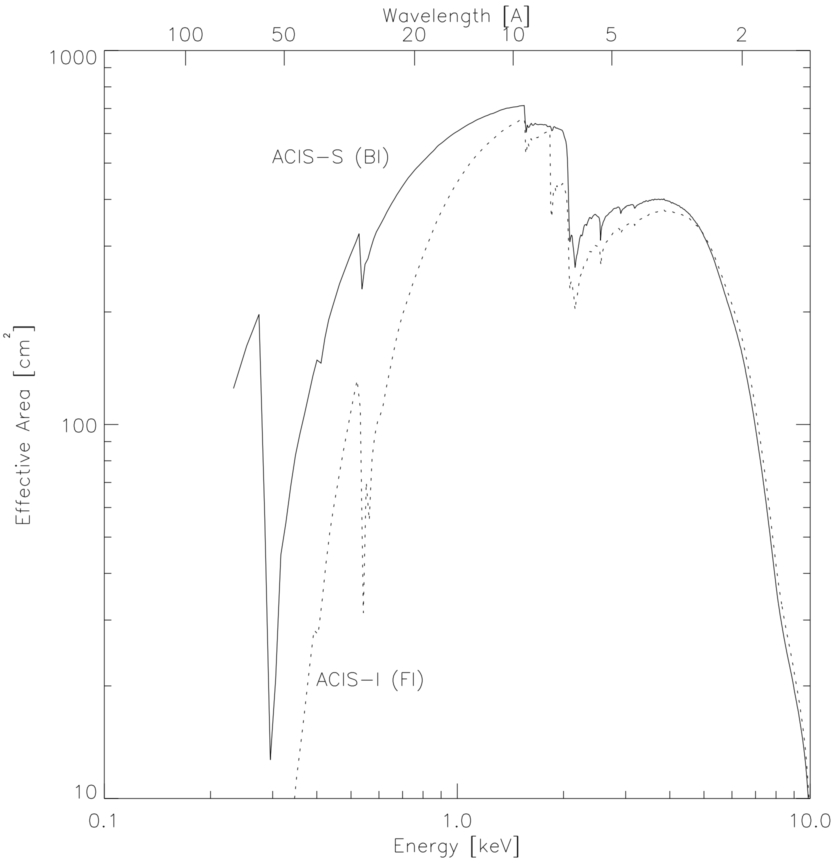

Figure B.7: The predicted effective area for the ACIS-S array versus energy. The dashed line is for the front-illuminated chips, the solid line for the back-illuminated ones (Taken from the CHANDRA Proposers' Observatory Guide at the URL: `http://cxc.harvard.edu/udocs/docs/docs.html`.)

This leads to a variable effective mirror area with respect to the photon energy. This effect is also the reason for the different sizes of the four CHANDRA mirrors: The small inner mirrors focus the hard X-rays, whereas the effective area of the outer mirrors is bigger for the soft X-rays. The interaction of the incoming photons with the detector medium is another instrumental effect that determines the measured spectra. Especially the probability of detecting a photon in a CCD chip, the quantum efficiency, depends on the photon energy. In Figure B.7 the predicted effective area of the ACIS-S array is plotted as a function of photon energy. This function represents the spectral response of the detector to a flat (equal number of incoming photons per energy unit) continuum source. A measured spectrum thus will always be the convolution of this response function with the true, intrinsic source spectrum.

CHANDRA observed NGC 1052 on August 28th, 1999 with an exposure time of 2400 s with the ACIS-S detector configuration. The experiment was planned and scheduled by Dr. G. P. Garmire. After the proprietary period of one year the obtained data has been included in the public data archive[3] from which it was downloaded for analysis. The further

[3]Data from the public CHANDRA data archive can be obtained via the graphical, java based user interface ChaSer (available under `http://cxc.harvard.edu/cda/chaser.html`) or directly at the provisional

processing of the data was done by Dr. J. Kerp with the "CHANDRA Interactive Analysis of Observations" program (CIAO)[4]. A color coded image of NGC 1052 was produced, in which the soft (0.1-1 keV), medium (1-2 keV) and hard (2-3 keV) photon detections are represented by red, green and blue pixels. The technique of adaptive smoothing was used, that spreads the area of a presumed source in the image as far as necessary to reach a specified statistically reliability of the detection. A clipping level of 3σ was chosen. In appendix D the resulting image is presented and discussed.

web interface under `http://cxc.harvard.edu/cgi-gen/cda/retrieve5.pl`.

[4]See `http://cxc.harvard.edu/ciao` for a detailed documentation of this software.

Appendix C

The radio jet of NGC 1052 on kpc–scales

The tapered MERLIN image of NGC 1052, obtained from the November 1995 observation, is shown in Figure C.1. The map is qualitatively very similar to the published image of Wrobel (1984). A very dominant compact core of 1 Jy is seen. Two lobes of extended emission extent about 15 arcsec east and west of the core. In both lobes there are regions of enhanced surface brightness (possibly two hot spots) with a P.A. of about 95°.

Figure C.2 shows the source restored with a circular beam of 1.7 arcsec and the VLA map of Wrobel (1984) from December 1980 with the same linear scale and restoring beam. The VLA, which was operated in its A configuration during the 1980 observations, was more sensitive to extended structures, which partially have been resolved out by MERLIN. Although some contribution by such extended structures might have been lost in the

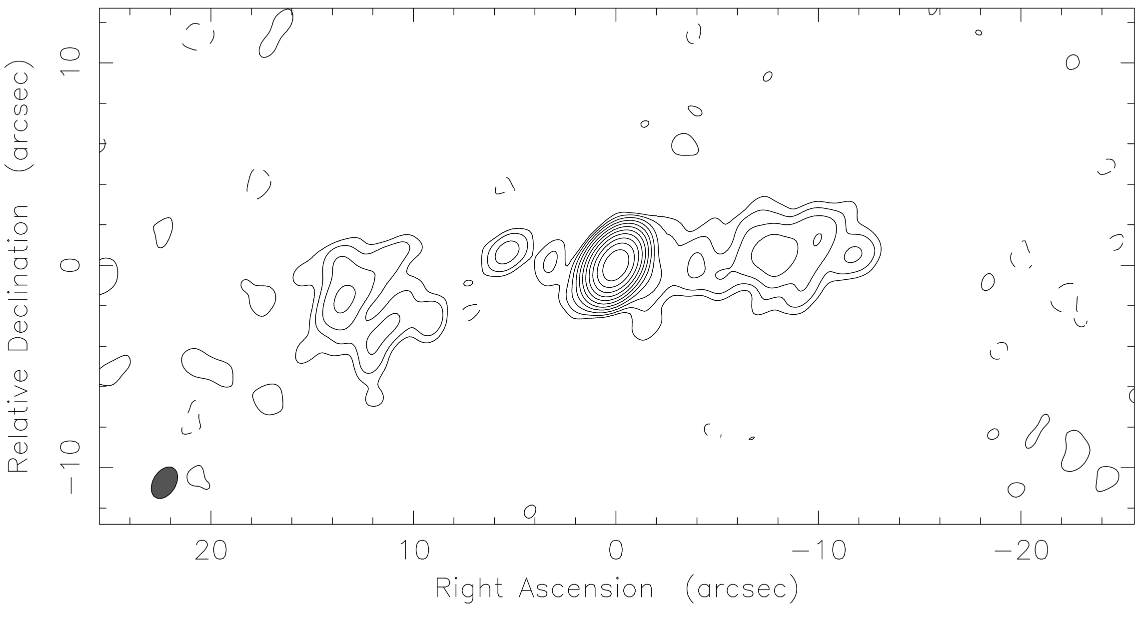

Figure C.1: NGC 1052 on arcseconds scale at 1.4 GHz as imaged by MERLIN. Contours at (−0.5, 0.5, 1, 2, 4, 8, 16, 32, 64, 128, 256, 512) × 1mJy are shown.

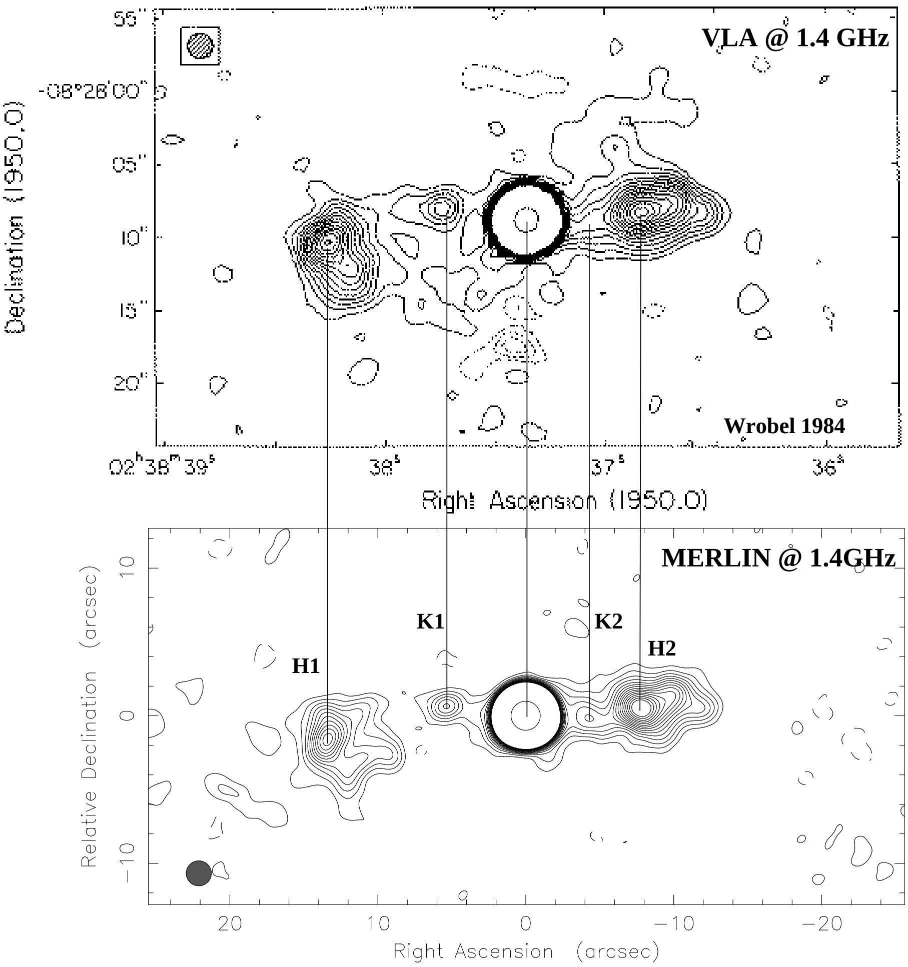

Figure C.2: Comparison between an 1984 VLA image of NGC 1052 (by Wrobel 1984) and the MERLIN image from 1995 at 1.4 GHz. Both maps have been convolved with the same (circular) restoring beam of 1.7 arcsec FWHM. Contours at (-1, 1, 2, 3, 4, 5, 6, 7, 8, 9, 10, 11, 12, 13, 14, 15, 800) × 0.5 mJy are given in both maps (The VLA map shows additionally negative contours at (−4, −3, −2) × 0.5 mJy). The hot spots (labeled as H1 and H2) do not show any motion. Two knots of emission (labeled as K1 and K2) have become significantly brighter (see text). The emission peak of the eastern knot (K1) additionally appears about half an arcsecond closer to the core in the (newer) MERLIN map. The core also brightened from 0.74 Jy to 1.01 Jy.

MERLIN image, it can be stated that the core has varied significantly, with a flux density of 740 mJy in December 1980 and 1 Jy in November 1995. The western hot spot (labeled as H2 in Figure C.2) has increased in flux density, as well as a knot in the western jet (labeled as K2), which was not visible as a local maximum in the 1980 VLA image.

By aligning the core positions at both epochs, the relative separations of the various features in the source can be compared. The hot spots H1 and H2 do not show significant positionally variations but a knot, about 5 arcsec from the core in the eastern jet (labeled as K1), has shifted about half an arcsecond inwards. A close examination of the second, pure naturally weighted MERLIN image (Figure C.3) reveals that this knot K1 is composed out of two separate sub-components (labeled as K1a and K1b). These are separated by the same distance of ∼0.5 arcsec, as the shift of the blended feature in Figure C.2 and

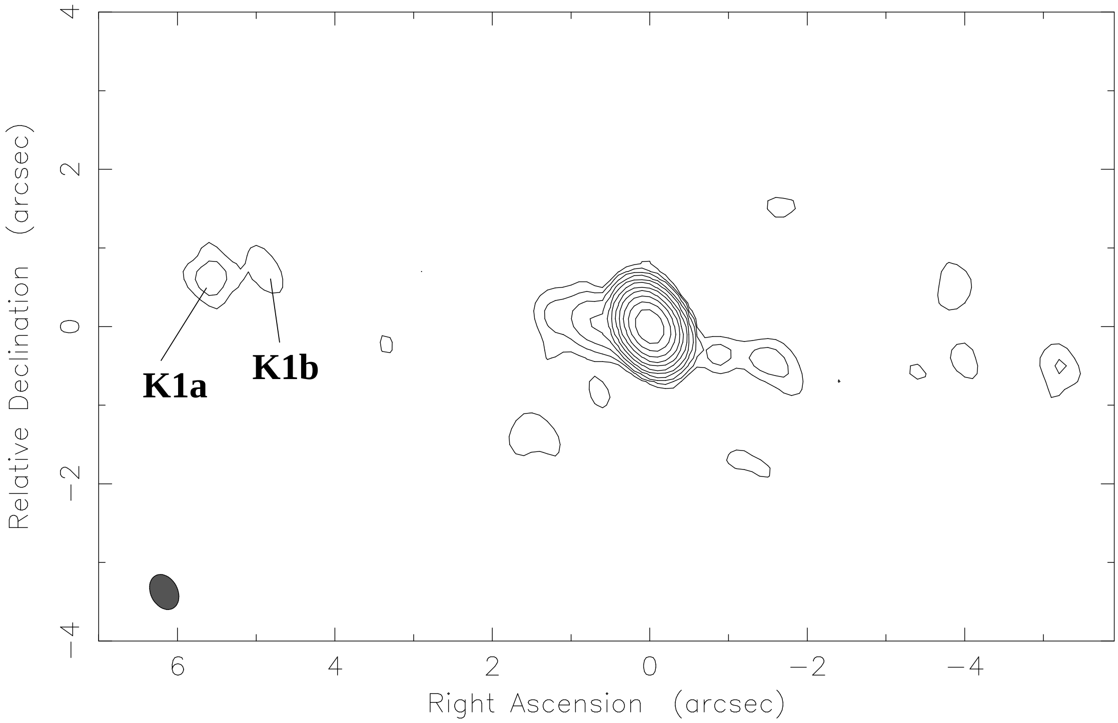

Figure C.3: The core of NGC 1052 with sub arcsecond resolution. The unresolved core has a peak flux density of 1 Jy per beam. Contours at (−0.5, 0.5, 1, 2, 4, 8, 16, 32, 64, 128, 256, 512) × 1 mJy are shown. Two sub components of knot K1 are resolved (labeled as K1a and K1b). Jet and counterjet emission can be seen up to ∼ 1.5 arcsecs from the core with a P.A. of 83° for the jet and −106° for the counterjet.

contribute comparable fractions to the combined flux density of K1. This implies that the inner sub-component K1b might have increased in flux density between 1980 and 1995, causing an apparent shift of K1. Since no high resolution 1980 image of NGC 1052 exists, this statement cannot be tested directly. Nevertheless, it appears more plausible than an inward motion of K1 by about 50 pc in 15 years, which would correspond to a jet speed of $\sim 10\,c$.

Figure C.3 shows for the first time the jet and the counterjet of NGC 1052 with sub–arcsecond resolution. The jet extends out to ∼1.5 arcsec with a P.A. of about 83°, comparable to the P.A. of the pc–scale jet. Weaker counterjet emission is also visible up to 2 arcsec west from the core. Its P.A. of ∼−106° agrees roughly with the P.A. on pc–scales, although a slight bending to the north is suggested.

The main purpose of the Merlin data within the scope of this thesis is to compare the radio structure of NGC 1052 on kpc–scales with the X-ray CHANDRA image, which will be done in Appendix D.

Appendix D

The X-ray jet of NGC 1052

The CHANDRA image of NGC 1052 is shown in Figure D.1. Strong X-ray emission from the AGN is seen in this image as well as diffuse extended emission well aligned with the radio jet, whose MERLIN image is superimposed in contours. This is the first direct detection of the X-ray jet of NGC 1052.

Close to the nucleus a tentative correlation between radio and X-ray emission can be found while the synchrotron emission in the radio lobes tends to anti-correlate with the X-ray intensity distribution. East and west of the core, there are two X-ray emitting regions, coinciding with enhanced brightness regions in the radio regime, which can also be seen in an optical image, taken by the Hubble Space Telescope (Pogge et al. 2000). The X-rays from these knots might be produced in a very different physical process than the more diffuse, extended emission. Synchrotron or inverse Compton radiation could be responsible for their brightness over this large frequency range but the poor photon statistics prevented the derivation of spectra of either knot to test this hypothesis.

To constrain the emission process of the X-ray jet, an annulus which excludes the nucleus itself but includes the whole area of the X-ray jet was selected. Two different models have been fitted to the jet–spectrum (see Figure D.2): a Raymond and Smith plasma (Raymond & Smith 1977) and a simple power–law. The power–law fit result of the X-ray jet is highly implausible, because of the extraordinary steep photon index of $\Gamma \geq 7$.

Because the radio as well as the X-ray jet are considered to be located deep inside the galaxy NGC 1052 itself, the amount of photoelectric absorption distributed along the line of sight has to be determined. Using the thermal source model, an attenuating column density of $N_{\rm HI} \simeq 3.5 \times 10^{21}\,{\rm cm}^{-2}$ is found. This value is about an order of magnitude higher than the galactic foreground column density belonging to the Milky Way of $N_{\rm HI} = 2 \times 10^{20}\,{\rm cm}^{-2}$ (Hartmann & Burton 1997). This additional X-ray attenuation can be attributed to weakly ionized gas located inside the galaxy itself. A plasma temperature of $kT = (0.5 \pm 0.2)\,{\rm keV}$ for the diffuse X-ray jet emission can be derived.

The X-ray spectrum of the nucleus: The nuclear X-ray spectrum was extracted up to a diameter of 2 arcsec. Comparing both X-ray spectra in Figure D.2 reveals the much softer X-ray emission of the jet. The bulk of the X-ray jet emission originates below $E < 2\,{\rm keV}$ while the X-ray spectrum of the nucleus has additional hard X-ray emission. ASCA as well as the ROSAT PSPC could not separate between the nucleus and the jet

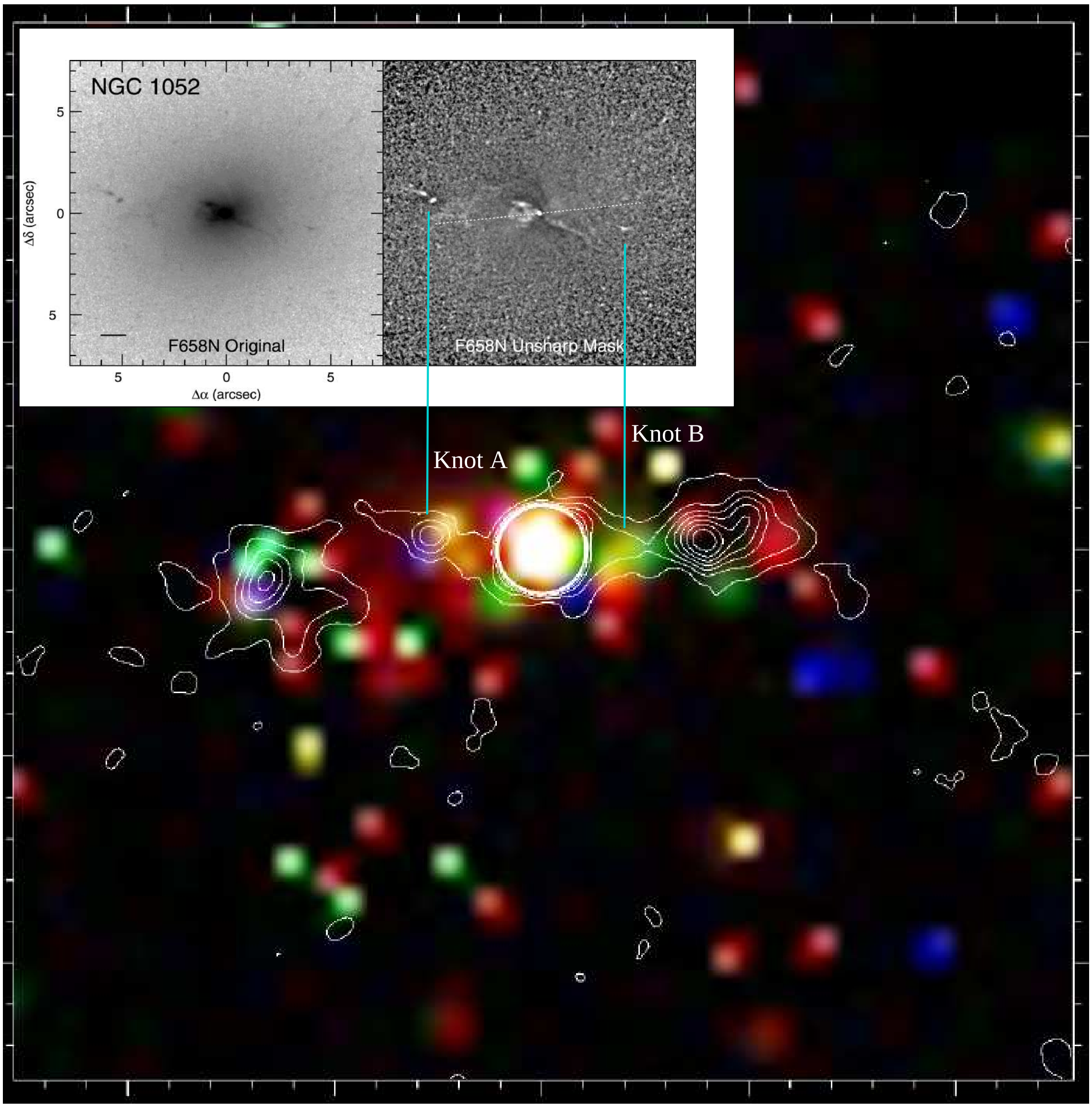

Figure D.1: The X-ray jet of NGC 1052 imaged by CHANDRA. The image has been smoothed to a resolution of 4″ to increase sensitivity. Each tick corresponds to 2″. Red represents photons between 0.1 and 1 keV, green between 1 and 2 keV and blue 2 to 3keV. The clipping level is 3σ. Overlaid are the contours of the 1.4 GHz Merlin map. The extended X-ray emission tends to anti-correlate with the radio-synchrotron emission. The jet emission is dominated by soft X-rays below 1 keV, whereas the AGN appears white representing a rather flat X-ray spectrum. The enclosed panel shows the optical jet (compare Figure 1.7) of NGC 1052, imaged with the HST by Pogge et al. (2000), on the same scale. Two knots, labeled as A and B, apear at the same positions as conspicuous peaks of the X-ray emission and regions of enhanced surface brightness in the radio band (K1 and K2 in the terminology of Appendix C).

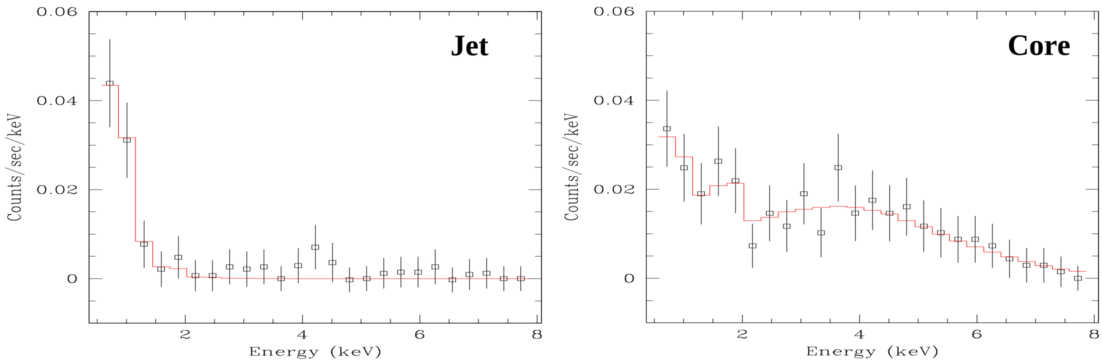

Figure D.2: X-ray spectrum of the jet (left panel) and core (right panel) of NGC 1052. The solid line indicates the best-fit model.

spatially but the soft X-ray emission of the jet was already detectable in terms of a soft excess of the X-ray spectrum in the PSPC data (see Weaver et al. 1999).

The soft X-ray emission below $E < 2\,\mathrm{keV}$ in the nuclear spectrum is at a comparable intensity level as the X-ray emission of the jet. Assuming that a fraction of the diffuse X-ray emission of the jet originates also in the extraction region of the nucleus, a hybrid model for the X-ray spectral approximation of the nuclear spectrum was used. The observed intensity distribution is written as

$$I_{\mathrm{obs}} = (I_{\mathrm{jet}} + I_{\mathrm{nucleus}} \times e^{-\sigma \times N_H(\mathrm{torus})}) \times e^{-\sigma \times N_H(\mathrm{gal.})} \tag{D.1}$$

where I_{jet} is the X-ray spectrum of the jet and I_{nucleus} is the spectrum of the nucleus. The photoelectric absorption produced by the torus is represented in Equation (D.1) by $e^{-\sigma \times N_H(\mathrm{torus})}$ while the X-ray absorption produced by the interstellar medium of the galaxy is $e^{-\sigma \times N_H(\mathrm{gal.})}$. A power–law type X-ray spectrum of the central X-ray source was assumed. The plasma temperature of the X-ray jet contribution as well as the foreground X-ray absorbing column densities were fixed to the values derived above. The best fit values are: $N_{\mathrm{H}}(\mathrm{torus}) = 0.8^{+1.5}_{-0.60} \times 10^{23}\,\mathrm{cm}^{-2}$ and $\Gamma = 0.38^{0.31}_{-0.21}$. The absorbed X-ray flux is $F_{\mathrm{X}}(0.3 - 8.0\,\mathrm{keV}) = (4.3 \pm 1.4) \times 10^{-12}\,\mathrm{erg\,s^{-1}\,cm^{-2}}$.

The derived $N_{\mathrm{H}}(\mathrm{torus})$ is rather low. Data of other X-ray observatories imply much higher values for both, the $N_{\mathrm{H}}(\mathrm{torus})$ as well as Γ (Weaver et al. 1999, Guainazzi & Antonelli 1999, Guainazzi et al. 2000) but these high torus column densities are not supported by the CHANDRA data. This apparent discrepancy between the CHANDRA data and previous X-ray observations concerning the photon index can be caused by the pile–up degradation ($\sim 30\,\%$) of the CHANDRA data. The nuclear X-ray spectrum might appear flatter than expected, because of the artificial hardening of the X-ray spectrum. Taking this into consideration, the derived results are consistent with the analysis of Weaver et al. (1999) who fitted the combined ROSAT and ASCA data – both are not affected by the pile–up – and derived in general steeper X-ray photon indices using a variety of models. The determined absorbing column density, however, is not so sensitive to the pile–up effect.

Substituting I_{nucleus} from a power–law to a thermal bremsstrahlung model gave no sufficient results. In all cases the temperature values exceed the upper temperature boundary of 1 MeV.

The CHANDRA data provide for the first time direct evidence for an X-ray jet in NGC 1052 perfectly correlated in extent with the well studied radio jet. The X-ray jet can be approximated best with thermal X-ray emission of a plasma with kT = 0.5 keV. This temperature is consistent with the thermal component found earlier by Weaver et al. (1999) using ASCA and ROSAT data. Its unabsorbed flux is $F_{\mathrm{X-ray\,jet}}(0.3 - 8.0\,\mathrm{keV}) = (1.7 \pm 0.8) \times 10^{-13}\,\mathrm{erg\,s^{-1}\,cm^{-2}}$, only 2% of the X-ray emission of the nucleus. Because of the strong pile–up degradation of the CHANDRA data, no firm conclusions on the X-ray spectrum of the nucleus can be deduced.

The absorbing column density of ionized material towards the approaching VLBI–jet derived from the brightness temperature distribution is of the order of $\sim 6{\cdot}10^{22}\,\mathrm{cm^{-2}}$. This is in a good agreement with the absorbing column density of neutral hydrogen ($0.8^{+1.5}_{-0.60} \cdot 10^{22}\,\mathrm{cm^{-2}}$) derived from X-ray spectroscopy of the compact X-ray core of NGC 1052.

Appendix E

NGC 1052 – The film

To give an visual impression of the full multi-frequency structure of NGC 1052 the aligned CLEAN maps were used to produce a movie from the aligned CLEAN models of the Difmap output, interpolating them with a linear model, creating FITS-images (Flexible Image Transport System, Wells et al. 1981) and producing GIF-files (Graphic Interchange Format) from these using the WIP package (Morgan 1995). The resulting set of GIF-files was concatenated using the program FMP (Fast Movie Processor, Copyright 1997-1999 R. Tibljas and Z. Nicolic).

There are two different versions of this movie available, one "Hollywood version" (`http://www.mpifr-bonn.mpg.de/staff/mkadler/hollywood_1052.avi`) which starts at 5 GHz with a field of view of 40 mas zooming into the center of the galaxy as the frequency is tuned up. In a second ("Ufa") version of the movie (`http://www.mpifr--bonn.mpg.de/staff/mkadler/ufa_1052.avi`) a fixed field of view and a fixed beamsize of 1×0.5 mas (corresponding to the resolution at 2 cm) was chosen. A close inspection of the "Ufa" version of the film shows clearly the stationary emission regions in the outer parts of both jets fading away towards higher frequencies, the region B showing up at the base of the western jet above 5 GHz and the core of the eastern jet moving inwards slowly as expected in the case of a conical jet model (see Section 4.6). The choice of 1×0.5 mas for the beam makes the movie superresolved below 15 GHz. For this reason one has to be careful in order not to overinterprete this part. However, the movie is still a valid representation of the dynamics of the derived model which is not bordered by a special beamsize.

Two sequences of frames from each version of the movie are shown in Figure E.1. In various sections of this thesis the movie can be used as a helpful tool to visualize the discussed effects (opacity changes in various jet regions, core shift). As it exhibits clearly many aspects of general jet physics the movie is also meant to serve as an educational tool.

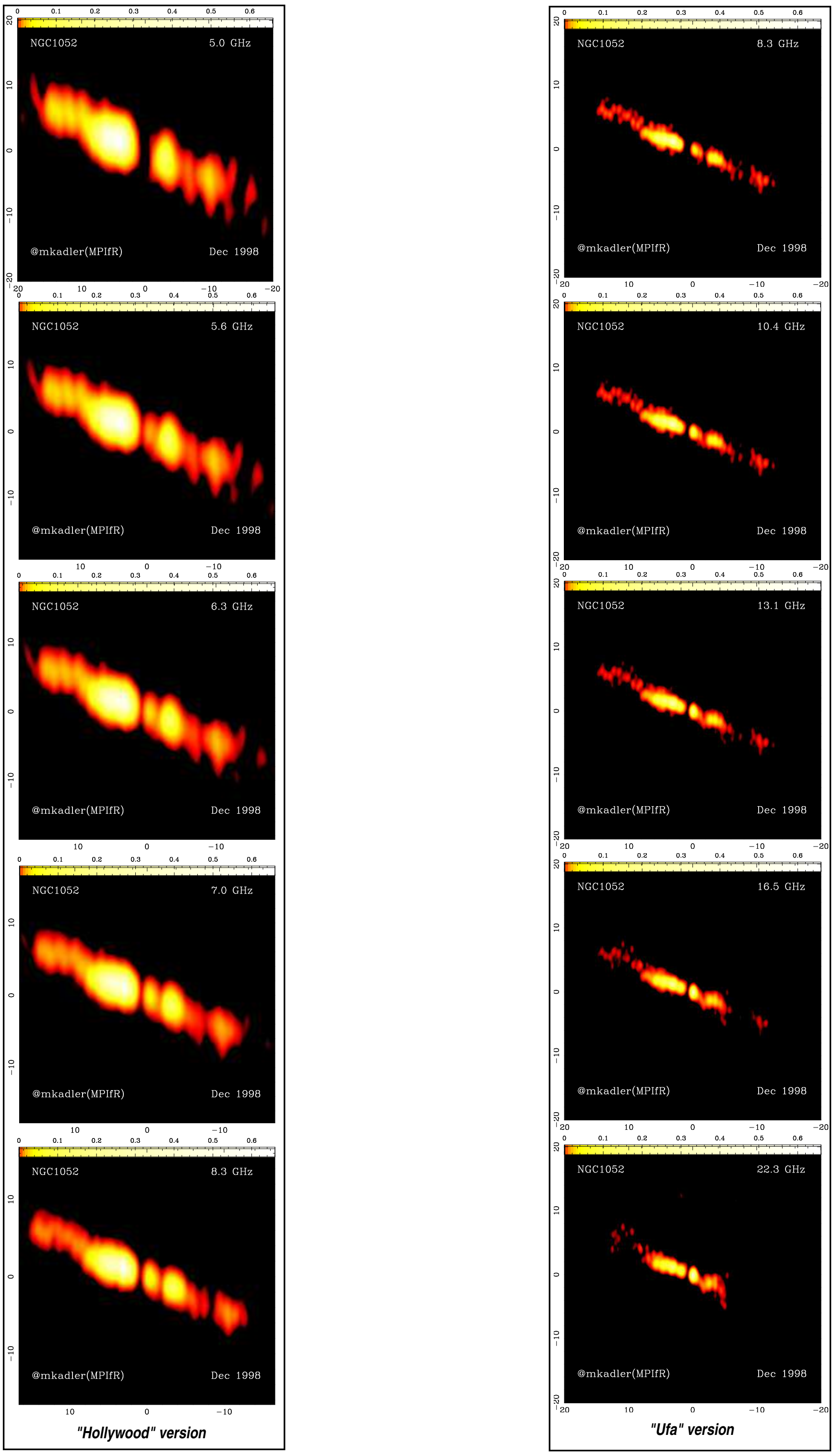

Figure E.1: Sequences of frames from the two versions of the NGC 1052-movie. Left panel: 5 frames from the "Hollywood" version of the film, showing the source evolution from 5 to 8.4 GHz. The field of view and the beam size are optimized for the special frequency of each frame. The appearance of component B at the core of the western jet is seen very clearly. Right panel: 5 frames from the "Ufa" version of the film between 8.4 and 22 GHz. The field of view is kept fixed for a better comparison of positional shifts with frequency. The beam size corresponds to the VLBA-beam at 15 GHz. The core shift in the eastern jet is very pronounced and positionally stationary features in the outer parts of both jets fade away towards higher frequencies (optically thin regime). Both movies can be obtained in the Internet from the URLs: `http://www.mpifr-bonn.mpg.de/staff/mkadler/zoom_1052.avi`, respectively `http://www.mpifr-bonn.mpg.de/staff/mkadler/ufa_1052.avi`.

Bibliography

Barth, A. J., Filippenko, A. V., & Moran, E. C. 1999, Astrophys. J., 515, L61

Becklin, E. E., Tokunaga, A. T., & Wynn-Williams, C. G. 1982, Astrophys. J., 263, 624

Blandford, R. D. & Königl, A. 1979, Astrophys. J., 232, 34

Blumenthal, G. R. & Gould, R. J. 1970, Reviews of Modern Physics, 42, 237

Braatz, J. A., Wilson, A. S., & Henkel, C. 1996, Astrophys. J. Suppl., 106, 51

Brown, R. L. 1987, in Spectroscopy of Astrophysical Plasmas, 35–58

California Institute of Technology. 1991, BAAS, 23, 991

Claussen, M. J., Diamond, P. J., Braatz, J. A., Wilson, A. S., & Henkel, C. 1998, Astrophys. J., 500, L129

Condon, J. J., Condon, M. A., Gisler, G., & Puschell, J. J. 1982, Astrophys. J., 252, 102

Daly, R. A. & Marscher, A. P. 1988, Astrophys. J., 334, 539

de Vries, W. H., Barthel, P. D., & O'Dea, C. P. 1997, Astron. & Astrophys., 321, 105

Eckart, A. & Genzel, R. 1996, Nature, 383, 415

Falcke, H. & Biermann, P. L. 1995, Astron. & Astrophys., 293, 665

Falcke, H., Wilson, A. S., & Simpson, C. 1998, Astrophys. J., 502, 199

Fomalont, E. 1981, Newsletter. NRAO No. 3, p. 3, 1981, 3, 3

Forbes, D. A., Georgakakis, A. E., & Brodie, J. P. 2001, Monthly Not. Roy. Astron. Soc., 325, 1431

Fosbury, R. A. E., Mebold, U., Goss, W. M., & Dopita, M. A. 1978, Monthly Not. Roy. Astron. Soc., 183, 549

Gómez, J. L., Marscher, A. P., Alberdi, A., Jorstad, S. G., & García-Miró, C. 2000, Science, 289, 2317

Gabel, J. R., Bruhweiler, F. C., Crenshaw, D. M., Kraemer, S. B., & Miskey, C. L. 2000, Astrophys. J., 532, 883

Gallagher, J. S. 1986, Publ. Astron. Soc. Pacific, 98, 81

Georganopoulos, M. & Marscher, A. P. 1996, in ASP Conf. Ser. 100: Energy Transport in Radio Galaxies and Quasars, 67

Guainazzi, M. & Antonelli, L. A. 1999, Monthly Not. Roy. Astron. Soc., 304, L15

Guainazzi, M., Oosterbroek, T., Antonelli, L. A., & Matt, G. 2000, Astron. & Astrophys., 364, L80

Harris, D. E., Carilli, C. L., & Perley, R. A. 1994, Nature, 367, 713

Harris, D. E. & Krawczynski, H. 2002, Astrophys. J., 565, 244

Hartmann, D. & Burton, W. B. 1997, Atlas of galactic neutral hydrogen (Cambridge; New York: Cambridge University Press)

Heeschen, D. S. 1970, Astron. J., 75, 523

Heeschen, D. S. & Puschell, J. J. 1983, Astrophys. J., 267, L11

Ho, L. C., Filippenko, A. V., & Sargent, W. L. 1995, Astrophys. J. Suppl., 98, 477

Ho, L. C., Filippenko, A. V., & Sargent, W. L. W. 1997, Astrophys. J. Suppl., 112, 315

Högbom, J. A. 1983, in Indirect Imaging. Measurement and Processing for Indirect Imaging. Proceedings of an International Symposium held in Sydney, Australia, August 30-September 2, 1983. Editor, J.A. Roberts; Publisher, Cambridge, England, New York, USA, Cambridge University Press, 1984, 247

Johnston, K. J., Fey, A. L., Zacharias, N., Russell, J. L., Ma, C., de Vegt, C., Reynolds, J. E., Jauncey, D. L., Archinal, B. A., Carter, M. S., Corbin, T. E., Eubanks, T. M., Florkowski, D. R., Hall, D. M., McCarthy, D. D., McCulloch, P. M., King, E. A., Nicolson, G., & Shaffer, D. B. 1995, Astron. J., 110, 880

Jones, D. L., Tingay, S. J., Murphy, D. W., Meier, D. L., Jauncey, D. L., Reynolds, J. E., Tzioumis, A. K., Preston, R. A., McCulloch, P. M., Costa, M. E., Kemball, A. J., Nicolson, G. D., Quick, J. F. H., King, E. A., Lovell, J. E. J., Clay, R. W., Ferris, R. H., Gough, R. G., Sinclair, M. W., Ellingsen, S. P., Edwards, P. G., Jones, P. A., van Ommen, T. D., Harbison, P., & Migenes, V. 1996, Astrophys. J., 466, L63

Jones, D. L., Wehrle, A. E., Meier, D. L., & Piner, B. G. 2000, Astrophys. J., 534, 165

Jones, D. L., Wrobel, J. M., & Shaffer, D. B. 1984, Astrophys. J., 276, 480

Kameno, S., Sawada-Satoh, S., Inoue, M., Shen, Z., & Wajima, K. 2001, Publ. Astron. Soc. Japan, 53, 169

Kellermann, K. I., Vermeulen, R. C., Cohen, M. H., & Zensus, J. A. 1999, in American Astronomical Society Meeting, Vol. 194, #20.02

Kellermann, K. I., Vermeulen, R. C., Zensus, J. A., & Cohen, M. H. 1998, Astron. J., 115, 1295

Kemball, A. J., Diamond, P. J., & Cotton, W. D. 1995, Astron. &. Astrophys. Suppl., 110, 383

Knapp, G. R., Faber, S. M., & Gallagher, J. S. 1978, Astron. J., 83, 139

Krichbaum, T. P., Alef, W., Witzel, A., Zensus, J. A., Booth, R. S., Greve, A., & Rogers, A. E. E. 1998, Astron. & Astrophys., 329, 873

Krolik, J. H. 1999, Active galactic nuclei : from the central black hole to the galactic environment (Princeton, NJ, USA : Princeton University Press, 1999.)

Leppänen, K. J., Zensus, J. A., & Diamond, P. J. 1995, Astron. J., 110, 2479

Levinson, A., Laor, A., & Vermeulen, R. C. 1995, Astrophys. J., 448, 589+

Lobanov, A. P. 1998, Astron. & Astrophys., 330, 79

Marr, J. M., Taylor, G. B., & Crawford, F. 2000, in Astrophysical Phenomena Revealed by Space VLBI, Proceedings of the VSOP Symposium, held at the Institute of Space and astronautical Science, Sagamihara, Kanagawa, Japan, January 19 - 21, 2000, Eds.: H. Hirabayashi, P.G. Edwards, and D.W. Murphy, Sagamihara, Kanagawa, Japan: Institute of Space and astronautical Science, 2000, 91

Mayall, N. U. 1939, Lick Observatory Bulletin, 497, 33

McDowell, J. C. 1994, in Einstein Obs. Unscreened IPC Data Archive

Mirabel, I. F. & Rodríguez, L. F. 1999, Annu. Rev. Astron. Astrophys., 37, 409

Miyoshi, M., Moran, J., Herrnstein, J., Greenhill, L., Nakai, N., Diamond, P., & Inoue, M. 1995, Nature, 373, 127

Morgan, J. A. 1995, in ASP Conf. Ser. 77: Astronomical Data Analysis Software and Systems IV, Vol. 4, 129

Napier, P. J. 1994, in IAU Symp. 158: Very High Angular Resolution Imaging, Vol. 158, 117

Omar, A., Anantharamaiah, K. R., Rupen, M., & Rigby, J. 2002, Astron. & Astrophys., 381, L29

Pearson, T. J., Shepherd, M. C., Taylor, G. B., & Myers, S. T. 1994, in American Astronomical Society Meeting, Vol. 185, #08.08

Peterson, B. M. 1997, An introduction to active galactic nuclei (Cambridge, UK, New York, USA: Cambridge University Press)

Pogge, R. W., Maoz, D., Ho, L. C., & Eracleous, M. 2000, Astrophys. J., 532, 323

Raymond, J. C. & Smith, B. W. 1977, Astrophys. J. Suppl., 35, 419

Ros, E. 1997, Astrometría diferencial de precisión con VLBI en el triángulo de Draco (y estudios de SN 1993J) (València, Spain: Servicio de Publicaciones, Universitat de València), 35

Rybicki, G. B. & Lightman, A. P. 1979, Radiative Processes in Astrophysics (New York, USA: Wiley-Interscience)

Schwartz, D. A., Marshall, H. L., Lovell, J. E. J., Piner, B. G., Tingay, S. J., Birkinshaw, M., Chartas, G., Elvis, M., Feigelson, E. D., Ghosh, K. K., Harris, D. E., Hirabayashi, H., Hooper, E. J., Jauncey, D. L., Lanzetta, K. M., Mathur, S., Preston, R. A., Tucker, W. H., Virani, S., Wilkes, B., & Worrall, D. M. 2000, Astrophys. J., 540, L69

Smith, D. A., Wilson, A. S., Arnaud, K. A., Terashima, Y., & Young, A. J. 2002, Astrophys. J., 565, 195

Thompson, A. R., Moran, J. M., & Swenson, G. W. 1986, Interferometry and synthesis in radio astronomy (New York, Wiley-Interscience)

Tingay, S. J. & Murphy, D. W. 2001, Astrophys. J., 546, 210

Van Gorkom, J. H., Knapp, G. R., Raimond, E., Faber, S. M., & Gallagher, J. S. 1986, Astron. J., 91, 791

Vermeulen, R. C., Readhead, A. C. S., & Backer, D. C. 1994, Astrophys. J., 430, L41

Vermeulen, R. C., Ros, E., Kellermann, K. I., Cohen, M. H., & Zensus, J. A. 2002, in prep.

Wagner, S. J. & Witzel, A. 1995, Annu. Rev. Astron. Astrophys., 33, 163

Weaver, K. A., Wilson, A. S., Henkel, C., & Braatz, J. A. 1999, Astrophys. J., 520, 130

Wells, D. C., Greisen, E. W., & Harten, R. H. 1981, Astron. &. Astrophys. Suppl., 44, 363

Wilson, A. S. & Yang, Y. 2002, Astrophys. J., 568, 133

Wilson, A. S., Young, A. J., & Shopbell, P. L. 2000, Astrophys. J., 544, L27

Wrobel, J. M. 1984, Astrophys. J., 284, 531

Young, A. J., Wilson, A. S., Terashima, Y., Arnaud, K. A., & Smith, D. A. 2002, Astrophys. J., 564, 176

Yusef-Zadeh, F., Melia, F., & Wardle, M. 2000, Science, 287, 85

Zensus, J. A. 1997, Annu. Rev. Astron. Astrophys., 35, 607

Zensus, J. A., Ros, E., Kellermann, K. I., Cohen, M. H., Vermeulen, R. C., & Kadler, M. 2002, in press (Astron. J., issue August 2002)